



ELSEVIER

Comput. Methods Appl. Mech. Engrg. 190 (2001) 2157–2179

**Computer methods  
in applied  
mechanics and  
engineering**

www.elsevier.com/locate/cma

# Implicit consistent and continuum tangent operators in elastoplastic boundary element formulations

Glaucio H. Paulino<sup>a,\*</sup>, Yong Liu<sup>b</sup>

<sup>a</sup> *Department of Civil and Environmental Engineering, University of Illinois, 2209 Newmark Laboratory, 205 North Mathews Avenue, Urbana, IL 61801-2352, USA*

<sup>b</sup> *Department of Mechanical Engineering, Aeronautical Engineering and Mechanics, Rensselaer Polytechnic Institute, Troy, NY 12180, USA*

Received 9 September 1998; received in revised form 5 January 2000

---

## Abstract

This paper presents an assessment and comparison of boundary element method (BEM) formulations for elastoplasticity using both the consistent tangent operator (CTO) and the continuum tangent operator (CON). These operators are integrated into a single computational implementation using linear or quadratic elements for both boundary and domain discretizations. This computational setting is also used in the development of a method for calculating the  $J$  integral, which is an important parameter in (nonlinear) fracture mechanics. Various two-dimensional examples are given and relevant response parameters such as the residual norm, computational processing time, and results obtained at various load and iteration steps, are provided. The examples include fracture problems and  $J$  integral evaluation. Finally, conclusions are inferred and extensions of this work are discussed. © 2001 Elsevier Science B.V. All rights reserved.

*Keywords:* Elastoplastic material; Consistent tangent operator; Continuum tangent operator; Boundary element method (BEM); Fracture mechanics;  $J$  integral

---

## 1. Introduction

Modeling of material nonlinear problems can be accomplished by, for example, the finite element method (FEM) or the boundary element method (BEM). Fig. 1 shows two meshes corresponding to application of each of these methods to a small-strain elastoplastic problem considering linear elements. Fig. 1(a) shows a possible mesh for the FEM, which requires discretization of the entire domain. Fig. 1(b) illustrates the modeling approach for the BEM, which is the method of choice in this work. Note that in addition to the boundary mesh (one-dimensional elements), domain cells (two-dimensional elements) are also needed, however, these cells are only required in regions of potential nonlinearity. If quadratic elements were employed in Fig. 1, the FEM mesh would have 144 elements (T6) and 323 nodes; and the corresponding BEM mesh would have 30 elements (3-noded) and 64 nodes (including 4 double nodes for corner modeling) on the boundary plus 36 elements (T6) in the interior and 95 nodes (27 on the boundary). Thus the boundary element treatment is best suited for nonlinear problems in which the size of the plastic zone is relatively small compared to the overall size of the finite domain. Moreover, the BEM is also advantageous

---

\* Corresponding author.

*E-mail address:* paulino@uiuc.edu (G.H. Paulino).

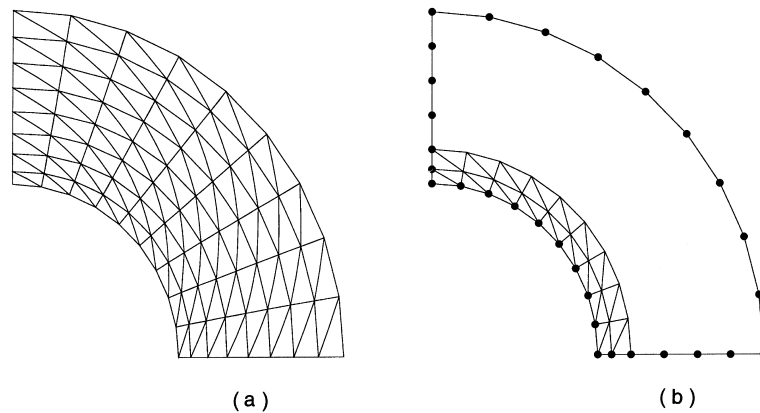


Fig. 1. Comparison of modeling strategies: (a) FEM mesh – 144 linear elements (T3) and 90 nodes; (b) BEM mesh – boundary discretization consists of 30 elements (2-noded) and 34 nodes (including four double nodes for corner modeling) on the boundary, and interior discretization consists of 36 linear elements (T3) and 30 nodes (14 on the boundary).

for unbounded domains containing a plastic region of finite extension, such as geotechnical problems involving tunnels and foundations.

This paper addresses two implicit algorithms, involving the consistent tangent operator (CTO) and the continuum tangent operator (CON) for the BEM modeling of small-strain elastoplastic problems. Most of the publications on BEM analysis of nonlinear problems in solid mechanics report on the use of continuum-based explicit and implicit approaches for “time” integration of the appropriate rate equations. Banerjee and his co-workers [1] have presented a variable stiffness continuum explicit formulation. Continuum implicit BEM formulations have been presented by Jin et al. [2], and Telles and Carrer [3,4]. Leu and Mukherjee [5,6] have presented continuum implicit objective integration schemes for recovery of stress sensitivities at a material point. Their work addresses large-strain viscoplastic problems, but only considers integration of the algorithmic constitutive model (somehow analogous to the radial return algorithm) at a material point. They have coupled this analysis with the BEM to solve general boundary value problems [7,8]. Application of the BEM to nonlinear (elastoplastic) fracture mechanics can also be found, for example, in the books by Cruse [9] and Leitão [10].

The CTO, however, has not been employed in the BEM before 1996. Bonnet and Mukherjee [11] were the first to present the CTO in implicit BEM for usual and sensitivity problems in elastoplasticity and, later on, Poon et al. [12] have developed a computational implementation for two-dimensional small-strain elastoplastic problems with isotropic hardening. They have shown that the converged value of the “global” CTO appears, as expected, as the “stiffness” matrix for the linear system of equations that govern the elastoplastic strain increment over a finite time step. The results obtained are very accurate as compared with analytical solutions and the FEM code ABAQUS.

However, the actual differences between CTO BEM and CON BEM have not yet been discussed further, not even in an example. This paper makes this comparison from nonlinear constitutive relations and BEM theory, and then integrates both CTO and CON into a single computer code using either linear or quadratic elements. This computational setting is further used in the development a method for evaluating the  $J$  integral considering elastoplastic fracture mechanics. This paper also provides a numerical comparison of different load and iteration steps during the nonlinear solution procedure. From this study, a good understanding of the techniques employed here can be obtained.

The goal for the remainder of this paper consists of developing a comprehensive presentation, and the next sections are organized as follows. First, some background is given and the basic notation and terminology is established. Next, the elastoplastic BEM formulation is derived in terms of both CTO and CON. Then, a method for computing the  $J$  integral, which is an important parameter in (nonlinear) fracture mechanics, is discussed in detail. Afterwards, the algorithm for the nonlinear computational procedure is presented and several numerical examples are given. The examples include crack problems and  $J$  integral evaluation. Subsequently, conclusions are inferred and directions for future work are discussed.

## 2. Basic concepts

This section reviews some relevant concepts and establishes the notation and terminology used herein. These concepts include constitutive law, *radial return algorithm* (RRA), CON, CTO, and Newton iteration method. The discussion below focuses on rate-independent plasticity with the von-Mises yield criterion and an associative flow rule. For the sake of simplicity, only isotropic hardening is considered in the present work. Kinematic hardening is accounted for by Paulino and Liu [13] in a BEM context, and by Simo and Taylor [14] in an FEM context.

Consider an Euclidean setting and define the displacement vector  $\mathbf{u} = u_i \mathbf{e}_i$ , where  $\mathbf{e}_i$  are the basis vectors and summation is applied to repeated indices. From standard kinematic considerations, the total strain tensor is obtained as the symmetric part of the displacement gradient tensor

$$\boldsymbol{\varepsilon} = \nabla^S \mathbf{u}, \tag{1}$$

in which  $\nabla^S = (\nabla + \nabla^T)/2$ , and the superscript T denotes the transpose. The stress tensor is denoted by  $\boldsymbol{\sigma} = \sigma_{ij} \mathbf{e}_i \otimes \mathbf{e}_j$ , where  $\otimes$  denotes the tensor product, and the local balance equations (in the absence of body forces) are

$$\nabla \cdot \boldsymbol{\sigma} = \mathbf{0}, \quad \boldsymbol{\sigma} = \boldsymbol{\sigma}^T. \tag{2}$$

Consider a computational plasticity setting and the evolution problem from a discrete incremental standpoint for a finite time step  $\Delta t$  (as opposed to continuous time). The elastoplastic constitutive law reduces to providing a rule which outputs  $\boldsymbol{\sigma}_{n+1}$  consistent with the yield criterion, for any given strain increment (input):

$$\Delta \boldsymbol{\varepsilon}_n = \boldsymbol{\varepsilon}_{n+1} - \boldsymbol{\varepsilon}_n, \tag{3}$$

such that

$$\boxed{\boldsymbol{\sigma}_{n+1} = \bar{\boldsymbol{\sigma}}(\boldsymbol{\varepsilon}_n, \boldsymbol{\sigma}_n, \bar{\boldsymbol{\varepsilon}}_n^p, \Delta \boldsymbol{\varepsilon}_n)}. \tag{4}$$

The notation  $\bar{\boldsymbol{\sigma}}$  symbolically denotes the action of the RRA [14,15] (which will be discussed later), the subscript  $n$  above refers to time (or pseudo-time)  $t_n$ ,  $\bar{\boldsymbol{\varepsilon}}^p$  is the cumulated equivalent plastic strain given by

$$\bar{\boldsymbol{\varepsilon}}^p = \int_0^t \sqrt{\frac{2}{3}} \|\mathbf{d}^p(\tau)\| \, d\tau, \tag{5}$$

where  $\mathbf{d}^p$  is the plastic strain rate tensor ( $\mathbf{d}^p = \dot{\boldsymbol{\varepsilon}}^p$ ), and

$$\|\mathbf{d}^p\| = [\mathbf{d}^p : \mathbf{d}^p]^{1/2} = +\sqrt{d_{ij}^p d_{ij}^p}. \tag{6}$$

Moreover,  $\text{tr}(\mathbf{d}^p) = 0$ , where  $\text{tr}(\cdot)$  denotes the trace operator.

Now let  $\mathbf{s}$  and  $\boldsymbol{\varepsilon}$  denote the deviatoric stress and strain tensors, which are given by

$$\mathbf{s} = \boldsymbol{\sigma} - \frac{1}{3}(\text{tr } \boldsymbol{\sigma})\mathbf{1} \quad \text{and} \quad \boldsymbol{\varepsilon} = \boldsymbol{\varepsilon} - \frac{1}{3}(\text{tr } \boldsymbol{\varepsilon})\mathbf{1}, \tag{7}$$

respectively, where  $\mathbf{1} = \delta_{ij} \mathbf{e}_i \otimes \mathbf{e}_j$ . The *yield condition* is

$$f(\mathbf{s}, \kappa) \equiv \|\mathbf{s}\| - \sqrt{\frac{2}{3}} \kappa(\bar{\boldsymbol{\varepsilon}}^p) = 0, \tag{8}$$

where  $\bar{\boldsymbol{\varepsilon}}^p \rightarrow \kappa(\bar{\boldsymbol{\varepsilon}}^p)$  is the hardening rule. The *consistency condition* reduces to the scalar equation

$$\mathcal{F}(\gamma \Delta t) \equiv \|\mathbf{s}_{n+1}^{\text{trial}}\| - \sqrt{\frac{2}{3}} \kappa(\bar{\boldsymbol{\varepsilon}}_{n+1}^p) - 2G[\gamma \Delta t] = 0, \tag{9}$$

where

$$\bar{e}_{n+1}^p = \bar{e}_n^p + \sqrt{\frac{2}{3}}[\gamma\Delta t], \tag{10}$$

and  $s_{n+1}^{\text{trial}}$  is the trial deviatoric stress given as

$$s_{n+1}^{\text{trial}} = s_n + 2G\Delta e_n, \tag{11}$$

in which  $G$  is the shear modulus of the material. Moreover, the notation  $\kappa(\bar{e}_n^p) = \kappa_n$  will be adopted in the development below. From a numerical point of view, the solution of Eq. (9), from which the values of  $[\gamma\Delta t]$  are determined, can be effectively accomplished by means of the the local Newton iteration procedure summarized below.

2.1. Determination of  $[\gamma\Delta t]$  using Newton iteration method

1. Let:  $\bar{e}_{n+1}^{p(k+1)} = \bar{e}_{n+1}^{p(k)} + \sqrt{(2/3)}\lambda^{(k)}$ , where  $\lambda = \gamma\Delta t$ .
2. Compute:  $D\mathcal{F}(\lambda^{(k)}) \equiv -2G[1 + (\kappa'/3G)]^{(k)}$ .
3. Perform iteration:  $\lambda^{(k+1)} = \lambda^{(k)} - (\mathcal{F}(\lambda^{(k)})/D\mathcal{F}(\lambda^{(k)}))$ .
4. Check convergence: If  $|\mathcal{F}(\lambda^{(k)})| > \text{EPS}$ , then  $k \leftarrow k + 1$ , and GOTO Step 1.

Here EPS is a prescribed tolerance indicating accuracy of the converged value, and  $D$  denotes the differential operator.

If  $f(s_{n+1}^{\text{tr}}, \kappa_n) \leq 0$ , then  $s_{n+1}^{\text{tr}}$  is elastic, and

$$\bar{\sigma} = K\Delta e_n : (\mathbf{1} \otimes \mathbf{1}) + 2G\Delta e_n + \sigma_n, \tag{12}$$

where  $K$  is the bulk modulus of the material. This is the elastic constitutive equation in incremental form. On the other hand, if  $f(s_{n+1}^{\text{tr}}, \kappa_n) > 0$ ,  $\bar{\sigma}$  is given by the following equations, which constitute the RRA.

2.2. Radial return algorithm

1. Compute trial elastic stress:  $s_{n+1}^{\text{trial}} = s_n + 2G\Delta e_n$ .
2. Compute unit normal:  $\hat{n} = s_{n+1}^{\text{trial}} / \|s_{n+1}^{\text{trial}}\|$ .
3. Use above converged value of  $[\gamma\Delta t]$  to compute equivalent plastic strain:  $\bar{e}_{n+1}^p = \bar{e}_n^p + \sqrt{2/3}[\gamma\Delta t]$ .
4. Compute the deviatoric stress:  $s_{n+1} = \sqrt{(2/3)}\kappa_{n+1}\hat{n}$ .
5. Add elastic volume change:  $\sigma_{n+1} = K\epsilon_{n+1} : (\mathbf{1} \otimes \mathbf{1}) + s_{n+1}$ .

Here,  $[\gamma\Delta t]$  solves Eq. (9). An illustration of the RRA is given in Fig. 2, where only the deviatoric components are shown and the actions take place on the  $\pi$ -plane. If the elastic trial stress  $s_{n+1}^{\text{trial}}$  and the stress  $\sigma_{n+1}^{(i)}$  at the  $i$ th iteration are computed from the nonconverged stress  $s_{n+1}^{(i-1)}$  at the previous iteration (rather than from converged stress  $s_n$  as above), then the CTO becomes a special case of the CON.

The expression for the CTO, which is the fourth-order tensor

$$\boxed{C_{n+1} = \frac{\partial \bar{\sigma}}{\partial \Delta e_n}}, \tag{13}$$

depends on the particular algorithm  $\delta e_n \rightarrow \sigma_{n+1}$  chosen. For the RRA presented here, it takes the form [14,15]

$$\boxed{C_{n+1}^{\text{ep}} = K\mathbf{1} \otimes \mathbf{1} + 2G\beta(\mathbf{I} - \frac{1}{3}\mathbf{1} \otimes \mathbf{1}) - 2G\bar{\gamma}\hat{n} \otimes \hat{n}}, \tag{14}$$

where  $\mathbf{I} = (1/2)[\delta_{ik}\delta_{jl} + \delta_{il}\delta_{jk}]e_i \otimes e_j \otimes e_k \otimes e_l$  and

$$\beta = \sqrt{\frac{2}{3}} \frac{\kappa_{n+1}}{\|s_{n+1}^{\text{trial}}\|}, \quad \bar{\gamma} = \frac{1}{1 + \frac{\kappa'}{3G}} - (1 - \beta). \tag{15}$$

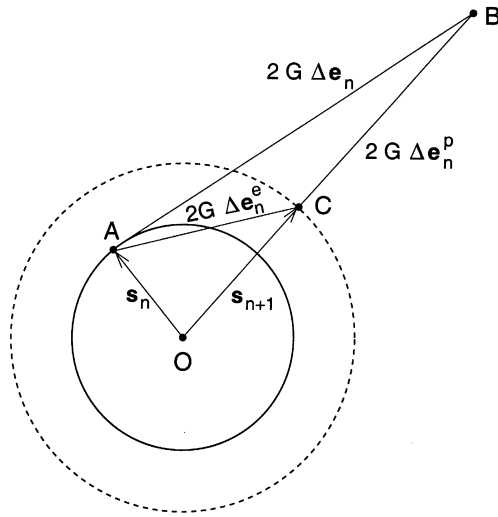


Fig. 2. Illustration of the RRA.

For the CON, its expression takes the common form used in FEM

$$\mathbf{C}_{n+1}^{ep} = K\mathbf{1} \otimes \mathbf{1} + 2G(\mathbf{I} - \frac{1}{3}\mathbf{1} \otimes \mathbf{1}) - 2G\gamma\hat{\mathbf{n}} \otimes \hat{\mathbf{n}}, \tag{16}$$

where

$$\gamma = \frac{1}{1 + \frac{k'}{3G}}. \tag{17}$$

Notice that in Eq. (14),  $\beta \leq 1$ , and that for a large time step  $s_{n+1}^{trial}$  may lay far out of the yield surface so that  $\beta$  may become significantly less than unity. In addition, because  $\bar{\gamma} = \gamma + \beta - 1$ , then  $\gamma - 1 < \bar{\gamma} \leq \gamma$ . Hence, for large time steps, the CTO, Eq. (14), may differ significantly from the CON, Eq. (16). It is interesting to observe that when the parameter  $\beta = 1$  in Eq. (14), the CTO becomes the CON, Eq. (16). As a result, use of the continuum operator in conjunction with the RRA, leads to loss of the quadratic rate of asymptotic convergence which characterizes Newton’s iteration method. This is the basic difference between CTO and CON methods.

It should be indicated that when  $\sigma_{n+1} = \bar{\sigma}(\epsilon_n, \sigma_n, \bar{e}_n^p, \Delta\epsilon_n)$  is elastic, one has

$$\mathbf{C}_{n+1} = \mathbf{C}_{n+1}^{ep} = \mathbf{C}, \tag{18}$$

where  $\mathbf{C}$  is the fourth-order tensor of elastic constants

$$\mathbf{C} = \lambda\mathbf{1} \otimes \mathbf{1} + 2\mu\mathbf{I}, \tag{19}$$

in which  $\mathbf{1}$  is the rank two tensor,  $\mathbf{I}$  is the rank four tensor (as given before), and  $\lambda$  and  $\mu$  are the Lamé constants of the material. Moreover,  $\mu \equiv G$ .

### 3. Elastoplastic boundary element formulation

An initial strain formulation for elastoplastic problems is adopted here. Next, the BEM representation at internal points is given and the global BEM CTO is presented. Then a brief discussion is provided on recovering the CON in the context of the present BEM formulation.

### 3.1. Initial strain formulation

Adoption of an initial strain formulation for elastoplasticity leads to the following regularized BIE [8]:

$$\int_{\partial\Omega} [u_i(\mathbf{z}) - u_i(\mathbf{x})] P_{ki}(\mathbf{x}, \mathbf{z}) \, dS_z - \int_{\partial\Omega} p_i(\mathbf{z}) U_{ki}(\mathbf{x}, \mathbf{z}) \, dS_z = \int_{\Omega} U_{ki,j}(\mathbf{x}, \mathbf{z}) C_{ijab} \varepsilon_{ab}^p(\mathbf{z}) \, dV_z, \quad (20)$$

without consideration of body forces. In Eq. (20),  $\mathbf{x}$  is any fixed point on the boundary  $\partial\Omega$ ;  $\Omega$  denotes the domain;  $U_{ki}, P_{ki}$  denote the components of the elastic singular kernels for displacement and traction (Kelvin kernels), respectively, i.e., those created in the infinite space  $\mathbb{R}^2$  by a unit point force applied at  $\mathbf{x}$  along the  $k$ -direction;  $\mathbf{p} = \boldsymbol{\sigma} \cdot \mathbf{n}$  is the traction vector; and the tensor  $\mathbf{C}$  is given by Eq. (19). Moreover, the variable field point is denoted by  $\mathbf{z}$  and  $(\cdot)_{,j} \equiv \partial(\cdot)/\partial z_j$ . The Kelvin kernels [16] are available in many references and can be found, for example, in Chapter 2, p. 46 of [8].

The matrix equation obtained from Eq. (20) can be written in symbolic form as

$$[\mathbf{H}]\{\mathbf{u}\} - [\mathbf{G}]\{\mathbf{p}\} = [\mathbf{Q}]\{\mathbf{C} : \boldsymbol{\varepsilon}^p\}. \quad (21)$$

In the standard BEM, the above equation is discretized and then recast as

$$[\mathbf{A}]\{\mathbf{y}\} = \{\mathbf{f}\} + [\mathbf{Q}]\{\mathbf{C} : \boldsymbol{\varepsilon}^p\}, \quad (22)$$

where  $\mathbf{y}$  collects the boundary unknowns and  $\{\mathbf{f}\}$  is the contribution of known boundary variables, i.e., values prescribed by the boundary conditions.

### 3.2. BEM representation at internal points

The displacement at an interior point is given by

$$u_k(\mathbf{x}) = \int_{\partial\Omega} p_i(\mathbf{z}) U_{ki}(\mathbf{x}, \mathbf{z}) \, dS_z - \int_{\partial\Omega} u_i(\mathbf{z}) P_{ki}(\mathbf{x}, \mathbf{z}) \, dS_z + \int_{\Omega} U_{ki,j}(\mathbf{x}, \mathbf{z}) C_{ijab} \varepsilon_{ab}^p(\mathbf{z}) \, dV_z. \quad (23)$$

Differentiation of the interior displacement integral equation with respect to  $x_\ell$ , and regularization [17], yields the representation formula for the displacement gradient

$$\begin{aligned} u_{k,\ell}(\mathbf{x}) = & \int_{\partial\Omega} u_i(\mathbf{z}) P_{ki,\ell}(\mathbf{x}, \mathbf{z}) \, dS_z - \int_{\partial\Omega} p_i(\mathbf{z}) U_{ki,\ell}(\mathbf{x}, \mathbf{z}) \, dS_z - C_{ijab} \varepsilon_{ij}^p(\mathbf{x}) \int_{\partial\Omega} n_\ell(\mathbf{z}) U_{ka,b}(\mathbf{x}, \mathbf{z}) \, dS_z \\ & - \int_{\Omega} U_{ki,j\ell}(\mathbf{x}, \mathbf{z}) C_{ijab} [\varepsilon_{ab}^p(\mathbf{z}) - \varepsilon_{ab}^p(\mathbf{x})] \, dV_z. \end{aligned} \quad (24)$$

The total strain at  $\mathbf{x}$  is then readily obtained from the above equation. In symbolic form, one has

$$\{\boldsymbol{\varepsilon}\} = [\mathbf{G}']\{\mathbf{p}\} - [\mathbf{H}']\{\mathbf{u}\} + [\mathbf{Q}']\{\mathbf{C} : \boldsymbol{\varepsilon}^p\} = -[\mathbf{A}']\{\mathbf{y}\} + \{\mathbf{f}'\} + [\mathbf{Q}']\{\mathbf{C} : \boldsymbol{\varepsilon}^p\}. \quad (25)$$

Substituting for  $\{\mathbf{y}\}$  from Eq. (22) into the above equation, one obtains

$$\{\boldsymbol{\varepsilon}\} = \{\mathbf{n}\} + [\mathbf{S}]\{\mathbf{C} : \boldsymbol{\varepsilon}^p\}, \quad (26)$$

where

$$\begin{aligned} \{\mathbf{n}\} &= \{\mathbf{f}'\} - [\mathbf{A}'][\mathbf{A}]^{-1}\{\mathbf{f}\}, \\ [\mathbf{S}] &= [\mathbf{Q}'] - [\mathbf{A}'][\mathbf{A}]^{-1}[\mathbf{Q}]. \end{aligned}$$

Note that  $\{\mathbf{n}\}$  denotes the purely elastic solution, i.e., the one obtained for the same loading but in the absence of plastic strain.

From Hooke's law and the additive decomposition of strain ( $\boldsymbol{\sigma} = \mathbf{C} : (\boldsymbol{\varepsilon} - \boldsymbol{\varepsilon}^p)$ ), one obtains

$$\{\mathbf{C} : \boldsymbol{\varepsilon}^p\} = \{\mathbf{C} : \boldsymbol{\varepsilon}\} - \{\boldsymbol{\sigma}\}, \quad (27)$$

which is incorporated in Eq. (26), giving

$$\{\boldsymbol{\varepsilon}\} = \{\boldsymbol{n}\} + [\mathbf{S}](\{\mathbf{C} : \boldsymbol{\varepsilon}\} - \{\boldsymbol{\sigma}\}). \quad (28)$$

Finally, the strain and the total stress are related through

$$[\mathbf{S}]\{\boldsymbol{\sigma} - \mathbf{C}\boldsymbol{\varepsilon}\} - \{\boldsymbol{n}\} + [\mathbf{I}]\{\boldsymbol{\varepsilon}\} = \{\mathbf{0}\}. \quad (29)$$

This development follows that of Refs. [3,11]. The above formulae for elastic problems with *initial* strain are given in accumulated form as opposed to rate form.

### 3.3. The global BEM CTO and CON

Consider the evolution of the continuum between time  $t_n$  and  $t_{n+1}$ . Using the notation  $\Delta(\cdot)_n = (\cdot)_{n+1} - (\cdot)_n$  and Eq. (29), one obtains

$$[\mathbf{S}]\{\Delta\boldsymbol{\sigma}_n - \mathbf{C}\Delta\boldsymbol{\varepsilon}_n\} - \{\Delta\boldsymbol{n}_n\} + [\mathbf{I}]\{\Delta\boldsymbol{\varepsilon}_n\} = \{\mathbf{0}\}, \quad (30)$$

which includes the equilibrium constraint.

On the other hand, the RRA, Eq. (4), relates  $\bar{\boldsymbol{\sigma}} = \boldsymbol{\sigma}_{n+1} = \boldsymbol{\sigma}_n + \Delta\boldsymbol{\sigma}_n$  to  $\Delta\boldsymbol{\varepsilon}_n$ . Combining the constitutive and equilibrium equations in the form

$$\{\boldsymbol{\sigma}_n\} + \{\Delta\boldsymbol{\sigma}_n\} = \{\bar{\boldsymbol{\sigma}}\},$$

one obtains a nonlinear equation for  $\Delta\boldsymbol{\varepsilon}_n$  of the form

$$\{\mathcal{G}(\Delta\boldsymbol{\varepsilon}_n)\} \equiv [\mathbf{S}]\{\bar{\boldsymbol{\sigma}}(\boldsymbol{\varepsilon}_n, \boldsymbol{\sigma}_n, \bar{\boldsymbol{\varepsilon}}_n^p, \Delta\boldsymbol{\varepsilon}_n) - \boldsymbol{\sigma}_n - \mathbf{C}\Delta\boldsymbol{\varepsilon}_n\} - \{\Delta\boldsymbol{n}_n\} + [\mathbf{I}]\{\Delta\boldsymbol{\varepsilon}_n\} = \{\mathbf{0}\}, \quad (31)$$

which has been written in a manner similar to Eq. (9). Thus, from a numerical point of view, the Newton method [18] can also be applied to Eq. (31). In this case, the correction  $\{\delta\boldsymbol{\varepsilon}_n^i\} = \{\Delta\boldsymbol{\varepsilon}_n^{i+1}\} - \{\Delta\boldsymbol{\varepsilon}_n^i\}$  to  $\{\Delta\boldsymbol{\varepsilon}_n^i\}$  solves

$$([\mathbf{S}][\mathbf{C} - \mathbf{C}_{n+1}^i] - [\mathbf{I}])\{\delta\boldsymbol{\varepsilon}_n^i\} = \{\mathcal{G}(\Delta\boldsymbol{\varepsilon}_n^i)\}. \quad (32)$$

Now let  $[\mathbf{D}_{n+1}^i] = [\mathbf{S}][\mathbf{C} - \mathbf{C}_{n+1}^i]$  so that

$$\boxed{[\mathbf{S}][\mathbf{C} - \mathbf{C}_{n+1}^i] - [\mathbf{I}] \equiv [\mathbf{D}_{n+1}^i] - [\mathbf{I}]}, \quad (33)$$

which is referred to as the global CTO by Mukherjee and co-workers [11,12] (see [19] for the FEM version). Note that the local CTO  $\mathbf{C}_{n+1}$  is given by Eq. (13). Once the nonlinear equation (31) is solved for  $\Delta\boldsymbol{\varepsilon}_n$ , all the variables at time  $t_{n+1}$  are readily computed. The Newton step, Eq. (32), involves the difference  $[\mathbf{C} - \mathbf{C}_{n+1}^i]$  between the elastic constitutive law and the local CTO, rather than the local CTO itself. This is consistent with the fact that Eq. (30) accounts for both equilibrium and elastic constitutive law, while for the FEM [14], only equilibrium is accounted for.

The elastic constitutive law and the local CTO differ only at points (referred to as “currently plastic”) where the current strain increment has a nonzero plastic component. Hence, it is convenient to rewrite the Newton step, Eq. (32), using a block decomposition:

$$([\mathbf{D}_{n+1}^i] - [\mathbf{I}])_{\text{PP}}\{\delta\boldsymbol{\varepsilon}_n^i\}_{\text{P}} = \{\mathcal{G}(\Delta\boldsymbol{\varepsilon}_n^i)\}_{\text{P}}, \quad (34)$$

$$\{\delta\boldsymbol{\varepsilon}_n^i\}_{\text{E}} = [\mathbf{D}_{n+1}^i]_{\text{EP}}\{\delta\boldsymbol{\varepsilon}_n^i\}_{\text{P}} - \{\mathcal{G}(\Delta\boldsymbol{\varepsilon}_n^i)\}_{\text{E}}. \quad (35)$$

The subscripts E, P indicate vectors and matrices restricted to the currently elastic (E) or plastic (P) nodes. Thus, only the restriction to currently plastic nodes of the global CTO  $([\mathbf{D}_{n+1}^i] - [\mathbf{I}])_{\text{PP}}$  needs to be factored. This shows that the global CTO has to be set up and factored only at currently plastic nodes, the currently elastic part  $\{\delta\boldsymbol{\varepsilon}_n^i\}_{\text{E}}$  being given explicitly by Eq. (35), after Eq. (34) is solved for  $\{\delta\boldsymbol{\varepsilon}_n^i\}_{\text{P}}$ . Moreover,

$$[D'_{n+1}]_{PE} = [D'_{n+1}]_{EE} = [0]. \tag{36}$$

The dimension of the linear system in Eq. (34) is directly associated to the size of the plastically deforming zone. This leads to an efficient solution scheme with savings in computing time.

The above process and equations for the CTO BEM are completely suitable for the CON BEM in elastoplasticity, where the RRA  $\bar{\sigma} = \sigma_{n+1}$  behaves in such a way that the stresses  $\sigma_{n+1}^{(i)}$  at the  $i$ th iteration are computed from the nonconverged stresses  $s_{n+1}^{(i-1)}$  at the previous iteration (i.e., with nonconverged  $[\gamma\Delta t]$ ), and the CTO parameter  $\beta = 1$ . This framework is adopted here.

**4. J integral – theory and implementation**

The  $J$  integral is accepted as a quasi-static fracture mechanics parameter for linear material response and, with limitations, for nonlinear material response [20,21]. This is one of a class of path-independent integrals that can be derived systematically for linearly elastic materials [22]. It is also path independent when the deformation theory of plasticity is used. The development below illustrates the application of  $J$  to elastoplastic materials, and its evaluation using the present BEM implementation. The  $J$  integral (see Fig. 3) is defined as

$$J = \int_{\Gamma_c} (W n_1 - p_i u_{i,1}) d\Gamma, \tag{37}$$

where  $n_1$  is the first component of the unit normal vector to  $\Gamma_c$ ,  $d\Gamma$  a length increment, and  $W$  is the strain energy density given by

$$W = \int_0^{\epsilon_{kl}} \sigma_{ij} d\epsilon_{ij} = W_E + W_P, \tag{38}$$

where  $W_E$  and  $W_P$  denote the elastic and plastic contributions to  $W$ , respectively. Moreover,

$$W_E = \frac{1}{2} \sigma_{ij} \epsilon_{ij}^e, \tag{39}$$

and

$$W_P = \int_0^{\bar{\epsilon}} \bar{\sigma} d\bar{\epsilon}^P. \tag{40}$$

The equivalent plastic strain  $\bar{\epsilon}^P$  is defined in Eq. (5) and the equivalent stress is given by

$$\bar{\sigma} = \sqrt{\frac{3}{2} \mathbf{s} : \mathbf{s}} = \sqrt{3J_2}, \tag{41}$$

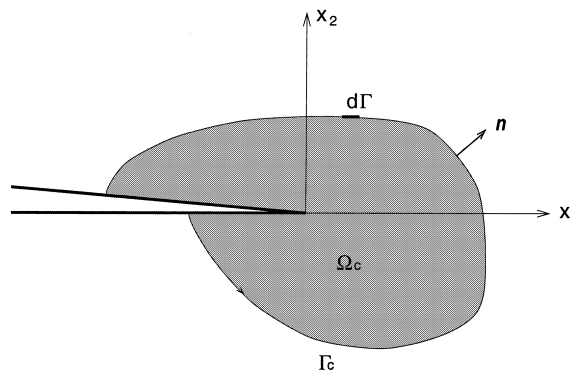


Fig. 3. Illustration of contour for  $J$  integral evaluation.

where  $J_2$  is the second invariant of the stress deviatoric tensor. Equation (41) is obtained from the first condition of Eq. (7) through the RRA (Eq. (4)).

The second term on the right-hand side of Eq. (37) is calculated as follows. The unknown tractions on the boundary at a certain load level are recovered from the vector  $\{y\}$  in Eq. (22), and the tractions on the contour chosen for  $J$  integral evaluation are obtained from  $\mathbf{p} = \boldsymbol{\sigma} \cdot \mathbf{n}$ . The term  $u_{1,1} \equiv \varepsilon_{11}$  is obtained directly from Eq. (25) for the internal strains, and the term  $u_{2,1}$  is obtained in a manner similar to Eq. (25), i.e.,

$$\{u_{2,1}\} = [\bar{\mathbf{G}}]\{\mathbf{p}\} - [\bar{\mathbf{H}}]\{\mathbf{u}\} + [\bar{\mathbf{Q}}]\{\mathbf{C} : \boldsymbol{\varepsilon}^p\}. \quad (42)$$

The unknown boundary quantities are obtained from the vector  $\{y\}$  in Eq. (22). Moreover,  $\{\mathbf{C} : \boldsymbol{\varepsilon}^p\}$  is obtained by means of Eq. (27). Because Eq. (42) is evaluated for all internal cells, the  $J$  contours can be defined for any path along the edges of the domain cells (interior elements).

If the  $J$  contour is chosen such that it passes through nodes of the domain cells, the evaluation of  $J$  is straightforward. For example, considering the three nodes of an edge of a quadratic triangular (or quadrilateral) cell, and applying Simpson's rule [18], one obtains

$$J^{\text{ec}} = h \left( \frac{1}{3}f_1 + \frac{4}{3}f_2 + \frac{1}{3}f_3 \right), \quad (43)$$

where  $J^{\text{ec}}$  denotes  $J$  for an edge of a cell,  $h$  is half the length of integration, and  $f$  is the integrand of Eq. (37) which is a function of  $W_E$ ,  $W_P$ ,  $\sigma_{i,j}$ , and  $u_{i,j}$  at each of the three points of the edge in consideration. The changes are little if other types of elements or integration schemes are used. All the relevant quantities are computed at each load step, and the final result is the sum of all the incremental contributions. Moreover, in order to account for the entire integration contour,

$$J = \sum_{i=1}^M J_i^{\text{ec}}, \quad (44)$$

where  $M$  is the number of cells that the selected contour passes through.

## 5. Computational algorithm

The discretization process for material nonlinear problems by means of the BEM involves both boundary elements and domain integration cells. Note, however, that the domain discretization is restricted to the potentially plastic region of  $\Omega$  (outside this region, no plastic strain is expected), as explained in Section 1. The following algorithm, based on Sections 2 and 3, is presented for solving the incremental elastoplastic problem, from the initial time  $t_0$  to the final time  $t_{(N_T)}$ . The initial time  $t_0$  is assumed to correspond to the first yield load.

**For**  $0 \leq n \leq (N_T - 1)$ :

1. Compute  $\{\Delta \mathbf{n}_n\}$  (purely elastic internal strain)
2. Initialize  $\{\Delta \boldsymbol{\varepsilon}_n^0\}$  (e.g., to the elastic value)

**Iterative solution of Eq. (31):**

- (2.1)  $i = 0$
- (2.2) Compute the residual  $\{\mathcal{G}(\Delta \boldsymbol{\varepsilon}_n^i)\}$  from Eq. (31).
- (2.3) Convergence test: if the condition in Eq. (45) is satisfied, **GOTO** 3.
- (2.4)  $i := i + 1$
- (2.5) Compute the local CTO or CON,  $\mathbf{C}_{n+1}^{\text{cp}}$ , at all nodes and determine the sets of currently elastic (E) and currently plastic (P) nodes.
- (2.6) Set up and factor the global CTO or CON,  $([\mathbf{D}_{n+1}^i] - [\mathbf{I}])_{\text{PP}}$ , and set up  $([\mathbf{D}_{n+1}^i] - [\mathbf{I}])_{\text{EP}}$ .
- (2.7) Solve Eq. (34) for  $\{\delta \boldsymbol{\varepsilon}_n^i\}_{\text{P}}$  and compute  $\{\delta \boldsymbol{\varepsilon}_n^i\}_{\text{E}}$  using Eq. (35).
- (2.8) Update:  $\{\Delta \boldsymbol{\varepsilon}_n^i\} := \{\Delta \boldsymbol{\varepsilon}_n^{i-1}\} + \{\delta \boldsymbol{\varepsilon}_n^i\}$ .
- (2.9) **GOTO** (b) (i.e., start new iteration).

## 3. Update:

- $\{\bar{\epsilon}^p\}_{n+1} = \{\bar{\epsilon}^p\}_n + \sqrt{\frac{2}{3}}\{[\gamma\Delta t]\},$
- $\{\sigma_{n+1}\} = \{\bar{\sigma}(\Delta\epsilon_{n+1}^i)\}.$
- $\{\epsilon_{n+1}\} = \{\epsilon_n\} + \{\Delta\epsilon_n\}$

**Continue**

Note that for the CTO,  $[\gamma\Delta t]$  is the converged value obtained by the Newton iteration method; for the CON,  $[\gamma\Delta t]$  is the unconverged value.

The convergence of the problem is measured in terms of the discrete residual norm (see Eq. (31)) for all the nodes, which is defined as

$$\|\{\mathcal{G}(\Delta\epsilon_n)\}\| \stackrel{\text{def}}{=} \sqrt{\frac{\sum\{\mathcal{G}(\Delta\epsilon_n)\}^2}{4N}} \leq \text{TOL}, \quad (45)$$

where  $N$  denotes the total numbers of nodes, and TOL is a specified tolerance. In this work,  $\text{TOL} = 5.0 \times 10^{-10}$  been found to be an adequate estimate for practical purposes. Unless otherwise stated, this value has been adopted for the examples presented in this work. While this tolerance may appear to be a severe condition to achieve, it will be shown by means of examples that this condition is easily satisfied when the CTO is used.

**6. Examples**

In order to provide a quantitative assessment of both the CTO BEM and the CON BEM, two groups of examples are investigated: a group which does not involve cracks (the first two examples) and a group involving cracks (the last three examples). The examples investigated are listed below:

1. Elastoplastic plate with a circular hole under uniaxial tension.
2. Elastoplastic hollow cylinder subjected to internal pressure.
3. Cracks emanating from a hole in an elastic plate.
4. Center-cracked elastoplastic plate.
5. Elastoplastic hollow cylinder with cracks emanating from the inner face.

Due to obvious symmetry reasons, only a quarter portion of the above problems is modeled. For the sake of simplicity, the Cartesian axes are referred as  $(x, y)$  rather than  $(x_1, x_2)$ . As usual, the linearly elastic example (#3) only requires boundary discretization (see Section 1). All the other examples are elastoplastic, and require discretization of the potentially plastic zone (see Fig. 1) in addition to the boundary discretization. Example #2 is solved using linear (2-noded boundary elements and 3-noded triangular internal cells) and quadratic (3-noded boundary elements and 6-noded triangular internal cells) interpolation of nodal quantities. All the other examples are solved using quadratic elements. Some of the nonlinear examples (e.g., the first two) are solved using a single load step. Use of a single load step is valid only for certain special situations, such as when every continuum point undergoes proportional loading. Thus, one should be careful in these situations. In general, repeating the analysis using more load steps and comparing the results is a more reliable strategy [12].

A preprocessing computer program to generate two-dimensional BEM meshes considering both boundary and domain discretization has been developed. In this preprocessor, the interior cells are generated by means of transfinite mapping. The main program for small-strain elastoplastic analysis contains both linear and quadratic elements, and double nodes are used to model corners and crack tips. All the computations in this work have been performed in an engineering workstation (Silicon Graphics – SGI).

*6.1. Plate with a circular hole under uniaxial tension*

Fig. 4 refers to a rectangular plate with a centered circular hole subjected to increasing extension under plane strain. This problem has been studied by Bonnet et al. [23], however, symmetry was not taken into account in order to avoid introduction of corners. They have modeled the entire plate and have

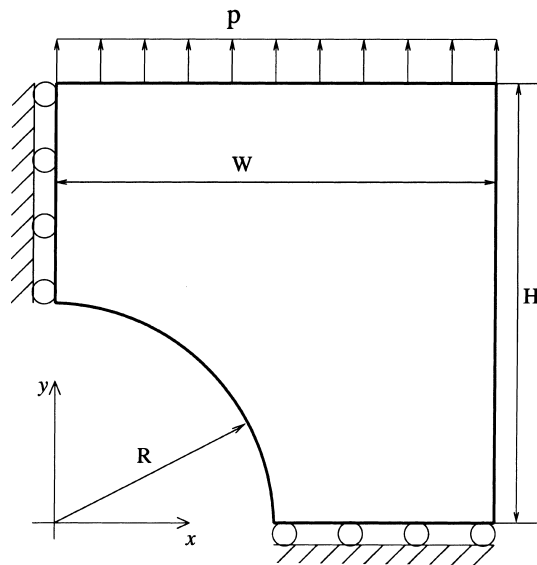


Fig. 4. Quarter portion of a plate with a centered circular hole subjected to uniaxial tension.

approximated each of the outer corners by a smooth ( $C^1$ ) arc. Here, only one quarter the plate is considered (see Fig. 4). The objective is to assess performance comparison between the CTO BEM and the CON BEM, and to show the significant loss in rate of convergence which occurs when the CON is used in place of the CTO (derived from the integration algorithm).

The numerical calculations are performed with 3-noded boundary elements and 6-noded triangular internal cells, as illustrated by Fig. 5. The elastic constants are  $G = 1.0$  and  $\nu = 0.3$ . Consistent units are used here. The material deforms according to the classical  $J_2$  plasticity theory, with isotropic hardening of the form

$$\kappa = 2G(0.001 + 0.001(\bar{\epsilon}^p)^m), \quad (46)$$

where the hardening exponent  $m = 0.0$  refers to the elastic perfectly plastic case. The initial tensile load is taken  $p = p_0 = 6.0 \times 10^{-4}$  so that a good portion of the sample has yielded. In order to compare the CTO and CON operators, various load and hardening parameters are used. The results obtained are summarized in Tables 1–4, and Figs. 6–8.

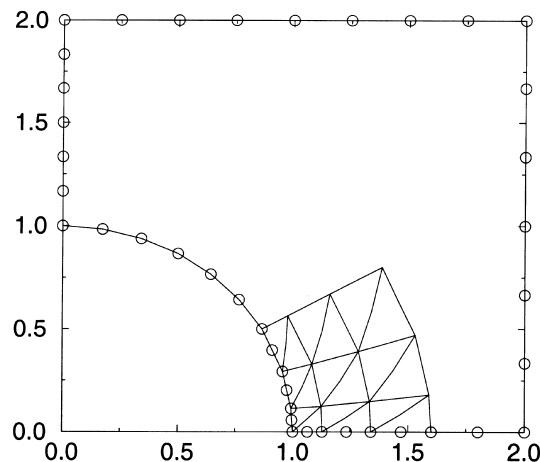


Fig. 5. BEM mesh for analysis of the plate with a hole under remote uniaxial tension. The boundary discretization consists of 20 quadratic elements and 45 nodes (including five double nodes for the corners); the domain discretization consists of 18 elements (T6) and 45 nodes.

Table 1

Comparison of CTO BEM and CON BEM with various hardening parameters<sup>a</sup> considering a single load step with  $p = p_0 = 6.0 \times 10^{-4}$ 

$m$	0.2	0.01	0.0001	0.00000001	0.000000
Iteration (CTO)	3	–	–	–	–
Iteration (CON)	23	23	22	22	–
CPU s (CTO) <sup>b</sup>	7.8	7.4	7.4	7.5	7.5
CPU s (CON) <sup>b</sup>	11.8	11.7	11.7	11.7	7.5
ResNorm (CTO)	3.497089E–10	1.827282E–11	1.827282E–11	1.827282E–11	1.766191E–11
ResNorm (CON)	2.035707E–09	3.917355E–10	3.857193E–10	3.709319E–10	1.766191E–11

<sup>a</sup>The special case with  $m = 0.0$  corresponds to elastic perfectly plasticity.<sup>b</sup>SGI workstation.

Table 2

Comparison of CTO BEM and CON BEM in 4 load steps with  $m = 0.2$  and  $p = p_0 = 6.0 \times 10^{-4}$ 

Load step	1	2	3	4
Iteration (CTO)	–	–	2	3
Iteration (CON)	–	–	9	22
CPU s (CTO) <sup>a</sup>	7.4	7.4	7.6	8.1
CPU s (CON) <sup>a</sup>	7.4	7.5	8.3	12.7
ResNorm (CTO)	4.4154784E–12	5.9490741E–12	3.8687151E–11	3.3372949E–10
ResNorm (CON)	4.4154784E–12	5.9490741E–12	3.6908099E–10	2.1643349E–09

<sup>a</sup>SGI workstation.

Table 3

Comparison of CTO BEM and CON BEM using a single load step and  $m = 0.2$  for various load levels<sup>a</sup> ( $p$ )

Load $p$	$0.8p_0$	$p_0$	$1.2p_0$	$1.4p_0$
Iteration (CTO)	2	3	4	5
Iteration (CON)	11	23	5	3
CPU s (CTO) <sup>b</sup>	7.5	7.8	8.4	9.3
CPU s (CON) <sup>b</sup>	8.6	11.8	9.2	9.1
ResNorm (CTO)	8.1470254E–11	3.4970898E–10	4.8204413E–11	7.9956174E–11
ResNorm (CON)	3.5013656E–10	2.0357074E–09 <sup>c</sup>	5.7704451E–06 <sup>c</sup>	1.8717323E–05 <sup>c</sup>

<sup>a</sup>The reference load is  $p_0 = 6.0 \times 10^{-4}$ .<sup>b</sup>SGI workstation.<sup>c</sup>Divergence occurs (cf. Eq. (45)).

Table 4

Comparison of the stress  $\sigma_y$  at  $y = 0.0$  ( $x$ -axis) obtained with CTO BEM and CON BEM using  $m = 0.2$  and  $p = 0.8p_0$ , where  $p_0 = 6.0 \times 10^{-4}$ 

$x$ -coordinate	$\sigma_y$ (CTO)	$\sigma_y$ (CON)
1.0000	0.26563E–02	0.22828E–02
1.0632	0.25873E–02	0.23662E–02
1.1263	0.21516E–02	0.23400E–02
1.2211	0.16911E–02	0.17662E–02
1.3158	0.13283E–02	0.13680E–02
1.4579	0.92692E–03	0.94415E–03
1.6000	0.58902E–03	0.59609E–03
1.8000	0.14249E–03	0.13847E–03
2.0000	–0.45574E–03	–0.47853E–03

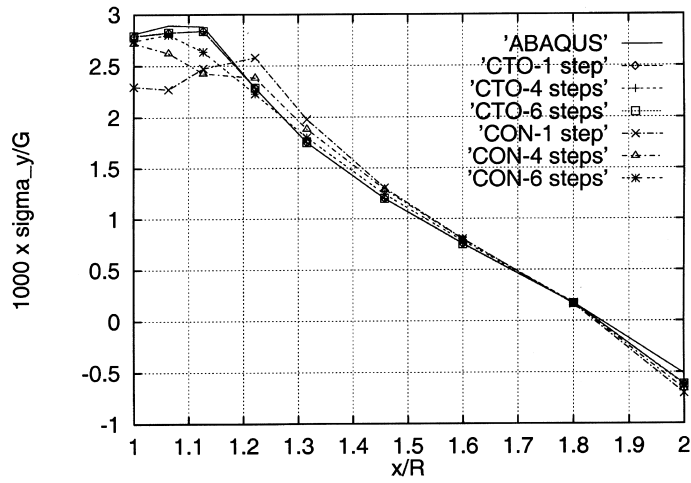


Fig. 6.  $\sigma_y$  vs.  $x/R$  at  $y = 0.0$ .

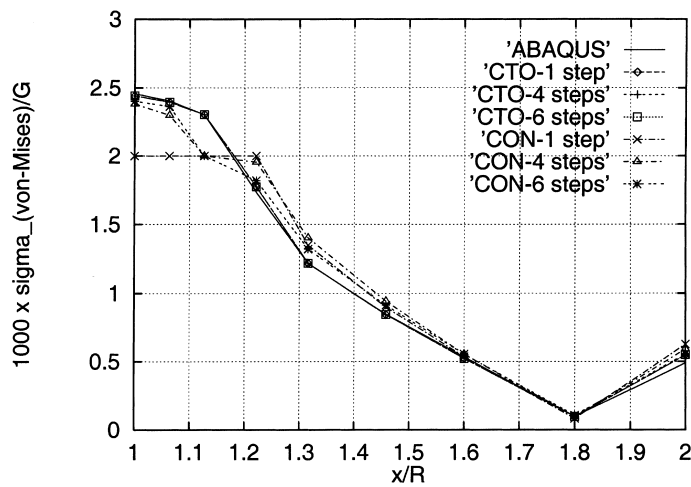


Fig. 7. Mises effective stress  $\bar{\sigma}$  vs.  $x/R$  at  $y = 0.0$ .

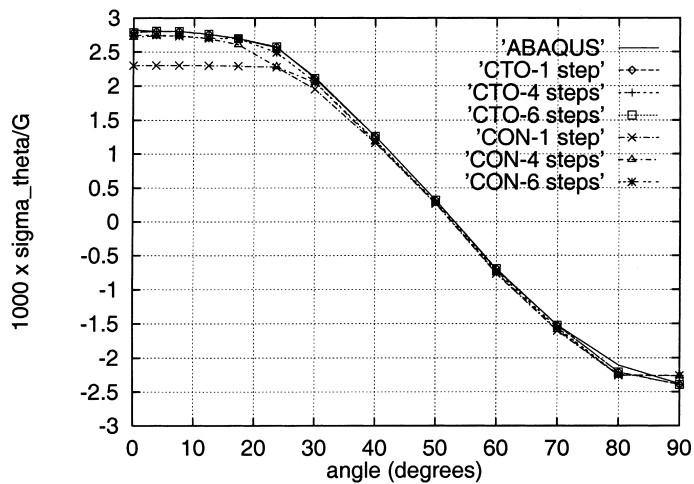


Fig. 8.  $\sigma_\theta$  at  $R = 1$  vs. the angle  $\theta$  along the circular hole boundary.

Tables 1–3 display the load steps, number of iterations, CPU time (seconds), and the residual norm (ResNorm) according to Eq. (45). As a general assessment, these tables show that the number of iterations for the CTO is much less than that required for the CON. Moreover, the residual norm (which provides a direct measure of how well the convergence condition given by Eq. (45) is satisfied), and CPU time for the CTO are also smaller than those for the CON. *This illustrates the practical importance of the CTO BEM in a Newton solution procedure.*

Table 1 provides a comparison of the CTO BEM and CON BEM with various hardening parameters  $m$ . Note that when  $m$  approaches zero (but is not precisely zero), there are no iterations for the results obtained with the CTO, but there are iterations with the CON. However, when  $m$  is actually zero (perfect plasticity case), both methods have no iterations. Table 2 shows a comparison of the CTO BEM and CON BEM at various load steps. Again, one can see that the CTO is clearly better than the CON with respect to number of iterations, CPU time, and residual norm. Table 3 shows a comparison of different load levels carried out in a single step. As the load increases, the results obtained with the CTO do converge according to the condition given by Eq. (45), however, those obtained with the CON only converge at relatively smaller loading levels. Note that only the smallest load, i.e.,  $p = 0.8p_0$ , leads to a fully converged result for the CON. This means that, in this example, the CTO can solve the nonlinear problem with large loading in just one load step, while the CON cannot. Therefore, the results for the CTO and CON in the last three columns of Table 3 should not be directly compared against each other because the CON does not satisfy the condition established by Eq. (45). Table 4 shows a comparison of the stress  $\sigma_y$  at  $y = 0.0$  obtained with both the CTO BEM and the CON BEM. The results agree relatively well with each other.

Figures 6–8 show a comparison of stresses obtained at several representative locations by means of the CTO BEM, CON BEM and the FEM code ABAQUS. The FEM discretization employs 8-noded quadrilateral elements (Q8) on a relatively fine mesh. Fig. 6 shows a comparison of the stress  $\sigma_y$  at  $y = 0.0$  as a function of  $x$ , Fig. 7 gives a comparison of the von-Mises effective stress  $\bar{\sigma}_{\text{Mises}}$  at  $y = 0.0$  along the  $x$ -axis, and Fig. 8 provides a comparison of the hoop stress  $\sigma_\theta$  along the inner face of the hole as a function of the angle  $\theta$  (see Figs. 4 and 5 for the problem description and discretization, respectively). From the plots in these three figures, one can verify that the results of the CTO in one, four, and six load steps agree very well; and these results are also close to the ABAQUS results. However, the CON results display relatively larger errors, especially for the one load step case. This might be due to the convergence accuracy (see Eq. (45)) – the residual norm for the CTO BEM is smaller than  $\text{TOL} = 5.0 \times 10^{-10}$ , while the CON BEM in one and four load steps cannot reach converged results within this tolerance. In fact, the CON reaches convergence with  $\text{TOL} = 5.0 \times 10^{-9}$ . However, when the CON takes six load steps, the results satisfy the same convergence criterion as the CTO BEM (i.e.,  $\text{TOL} = 5.0 \times 10^{-10}$ ). Figs. 6–8 show that the results of CON with six load steps are close to the results of both the CTO and the ABAQUS program.

## 6.2. Hollow cylinder subjected to internal pressure

Fig. 9 shows a hollow cylinder subjected to internal pressure, which deforms under plane strain conditions. This type of problem has been studied by Poon et al. [12] considering symmetry, and by Bonnet et al. [23], without consideration of symmetry (see related comments on the previous example). The hollow cylinder has inner radius 1 and outer radius 2. As before, the elastic constants are  $G = 1.0$  and  $\nu = 0.3$ . Consistent units are used here. This example also concerns hardening of the form established by Eq. (46), i.e.,

$$\kappa = 2G(0.001 + 0.001(\bar{\epsilon}^p)^m),$$

where  $m = 0.2$  (nonlinear strain hardening). The internal pressure is  $p = 12 \times 10^{-4}$ , resulting in a plastic front at roughly  $r = 1.15$  (where  $r$  denotes the radial distance). The internal cells extend to  $r = 1.2$ , which is far enough to cover the plastic zone. The entire load has been applied in a single load step.

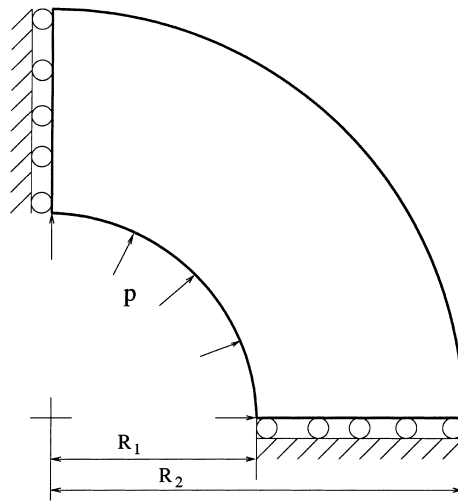


Fig. 9. Quarter portion of a hollow cylinder subjected to internal pressure loading.

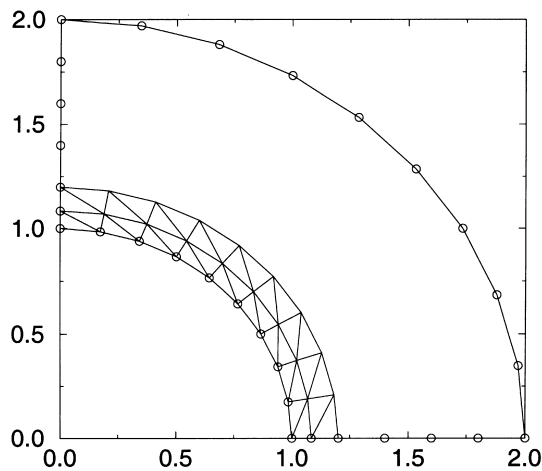


Fig. 10. BEM mesh for analysis of the hollow cylinder subjected to internal pressure. The boundary discretization consists of 30 linear elements and 34 nodes (including four double nodes for the corners); the domain discretization consists of 36 elements (T3) and 30 nodes.

Two meshes have been considered for this example, one using linear elements and the other using quadratic elements. The mesh with linear elements is shown in Fig. 10. For the mesh with quadratic elements, the boundary discretization consists of 30 elements and 64 nodes (including four double nodes for the corners); the domain discretization consists of 36 elements (T6) and 95 nodes. The mesh with linear elements (see Fig. 10) is essentially a stripped-down version of the mesh with quadratic elements (not shown here), where the intermediate nodes of all the quadratic elements (both on the boundary and in the interior of the domain) are absent.

Fig. 11 shows a comparison of hoop stress ( $\sigma_\theta$ ) along the  $\theta = 0$  radial segment (see Fig. 9) obtained with ABAQUS, the quadratic CTO (QCTO), and the linear CTO (LCTO). Here, “quadratic” and “linear” refer to the element type used in the BEM implementation. The ABAQUS solution is used as the reference result, and the FEM discretization consists of 8-noded quadrilateral elements (Q8) on a relatively fine mesh. Both the QCTO and LCTO agree reasonably well with the ABAQUS (reference) solution.

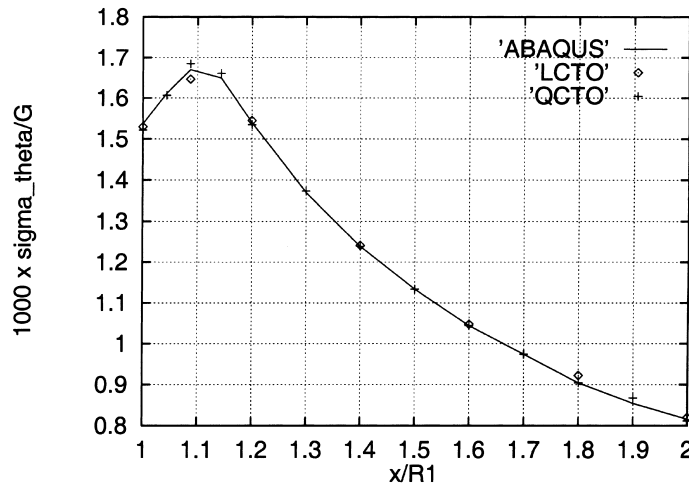


Fig. 11. Comparison of hoop stress ( $\sigma_\theta$ ) along the  $\theta = 0$  radial segment using ABAQUS (reference solution), quadratic CTO (QCTO), and linear CTO (LCTO). Here, “quadratic” and “linear” refer to the element type used in the BEM implementation.

### 6.3. Cracks emanating from a hole in an elastic plate

This example consists of verifying a linear elastic fracture mechanics (LEFM) problem that has been suggested as a benchmark problem by the “National Agency for Finite Element Methods and Standards” (NAFEMS). It is described in the NAFEMS publication “2D Test Cases in Linear Elastic Fracture Mechanics” and also in the ABAQUS Verification Manual [24]. This example is illustrated in Fig. 12, which refers to stretching of a rectangular plate with horizontal cracks on opposite sides of a centered circular hole. Due to symmetry reasons, only one quarter of the test geometry is modeled.

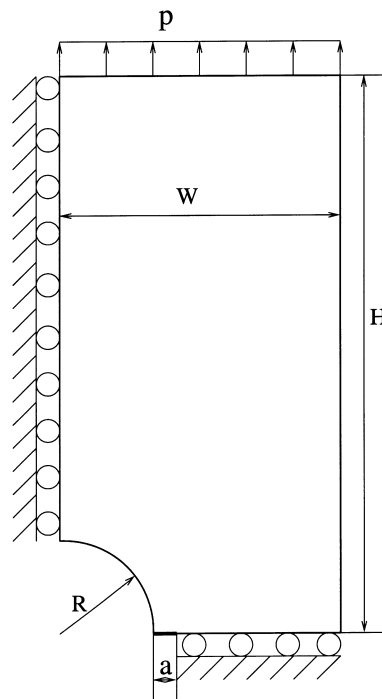


Fig. 12. Quarter portion of a plate with a crack emanating from the hole. The geometry satisfies the following relations:  $(R + a)/W = 0.3$ ,  $R/W = 0.25$ , and  $H/W = 2.0$ .

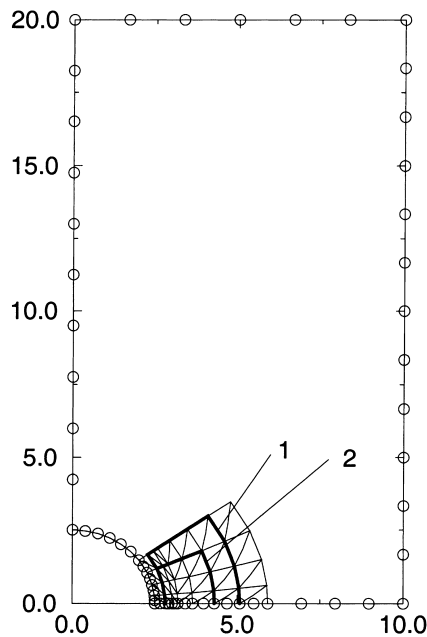


Fig. 13. BEM mesh for analysis of the elastic plate with a crack emanating from the hole. The boundary discretization consists of 30 quadratic elements and 66 nodes (including six double nodes for the corners and the crack tip); the domain discretization consists of 56 elements (T6) and 135 nodes. The two bold contours are used for  $J$  integral evaluation.

The numerical calculations are performed with 3-noded boundary elements and 6-noded triangular internal cells (used for  $J$  evaluation), as illustrated by Fig. 13. Note that the elements in the interior mesh change orientation at the crack tip. The material has Young's modulus  $E = 207$  GPa and  $\nu = 0.3$ . According to Fig. 12, the height is  $H = 20$  mm, the width is  $W = 10$  mm, the hole radius is  $R = 2.5$  mm, and the crack length is  $a = 0.5$  mm. The plate is loaded with a uniform tensile traction  $p = 100$  N/mm<sup>2</sup> acting on the top of the plate.

The target solution for the mode I stress intensity factor (SIF) is  $K_I/K_0 = 1.05$ , where  $K_0 = \sigma\sqrt{\pi a}$  (with  $\sigma = p$ ), and plane stress state is considered. In the plane strain BEM code, the  $J$  integral is evaluated on the contours shown in Fig. 13, and then the SIF is calculated in a postprocessing stage using  $K_I = \sqrt{JE(1-\nu^2)}$ . The results are itemized below:

- Target solution:  $K_I/K_0 = 1.05$ .
- Contour 1:  $K_I/K_0 = 1.131$ .
- Contour 2:  $K_I/K_0 = 1.016$ .

The average result of above two contours is 1.073, and thus the relative error with respect to the target solution is 2.19%. This example validates the present BEM scheme for solving a mode I LEFM problem.

#### 6.4. Center-cracked elastoplastic plane stress plate

Hellen [25] has presented a standard test consisting of a center-cracked plane stress plate with a crack length  $2a$ , width  $2W$ , ratio  $a/W = 0.2$ , and height  $2.5W$ . Hellen [25] has studied this problem using the FEM and Leitão [10] has used the BEM. Elastic perfectly plastic behavior, with yield stress  $\sigma_Y$ , is assumed, and a uniform load of magnitude  $p_n$  is applied normal to the edges, parallel to the crack axis. This example is illustrated by Fig. 14, where only one quarter of the test geometry is modeled.

The BEM mesh uses 3-noded boundary elements and 6-noded triangular internal cells, as illustrated by Fig. 15. Note that the elements in the interior mesh change orientation at the crack tip. The elastic constants of the material are Young's modulus  $E = 100,000$  MPa, and  $\nu = 0.3$ . The yield stress is  $\sigma_Y = 1,000$  MPa. The width of the plate is  $W = 100$  mm. The load is applied up to  $0.93p_n$ , where  $p_n = 0.8\sigma_Y$ .

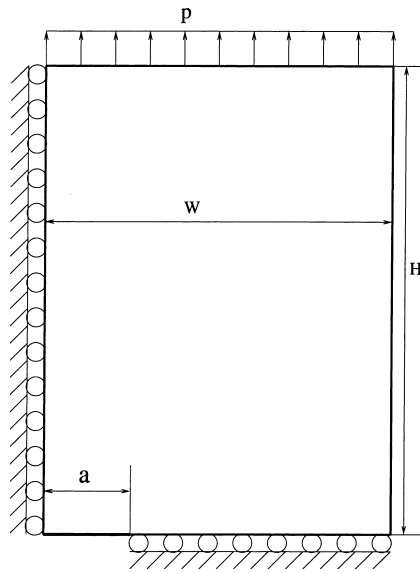


Fig. 14. Quarter portion of a plate with a centered crack subjected to uniaxial tension. The (semi-)crack length is  $a$ , the width is  $W$ , the height is  $H$ , and  $a/W = 0.2$ .

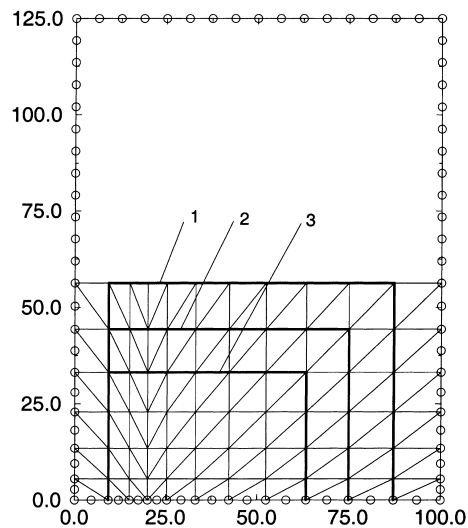


Fig. 15. BEM mesh for analysis of the plate with a centered crack. The boundary discretization consists of 43 quadratic elements and 91 nodes (including five double nodes for the corners and the crack tip); the domain discretization consists of 132 elements (T6) and 299 nodes. The three bold contours are used for  $J$  integral evaluation.

The results obtained are summarized in Fig. 16 and Table 5. The  $J$  integrals have been calculated in a manner analogous to the previous example. Fig. 16 shows a comparison of normalized  $J$  integral results obtained with the CTO BEM, the CON BEM, and those obtained by Leitão [10]. The present BEM results agree well with those by Leitão [10]. Although both the CTO and CON results are approximately the same, Table 5 shows that the number of iterations, CPU time, and residual norm (Eq. (45)) obtained with the CTO BEM are smaller than those obtained with the CON BEM. Thus, this example illustrates the superiority of the CTO BEM over the CON BEM for a fracture mechanics problem.

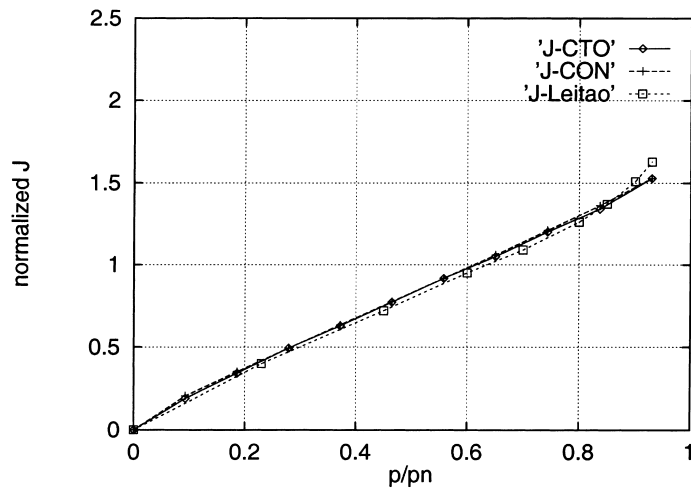


Fig. 16. Variation of the  $J$  integral with the load. Here  $J$  is normalized as  $\sqrt{(EJ)/(a\sigma_y^2)}$ .

Table 5  
Comparison of CTO BEM and CON BEM in 10 load steps

Load step	1–5	6	7	8	9	10
Iteration (CTO)	–	3	3	4	4	4
Iteration (CON)	–	7	8	12	18	19
CPU s (CTO) <sup>a</sup>	308.6	315.3	322.1	330.1	338.7	347.8
CPU s (CON) <sup>a</sup>	389.6	400.8	413.0	430.3	456.4	485.7
ResNorm (CTO)	7.2235E–11	9.6221E–11	1.0886E–10	1.2705E–10	1.6864E–10	2.1298E–10
ResNorm (CON)	7.2235E–11	1.2473E–10	3.9289E–10	4.7790E–10	3.6198E–10	3.8290E–10

<sup>a</sup>SGI workstation.

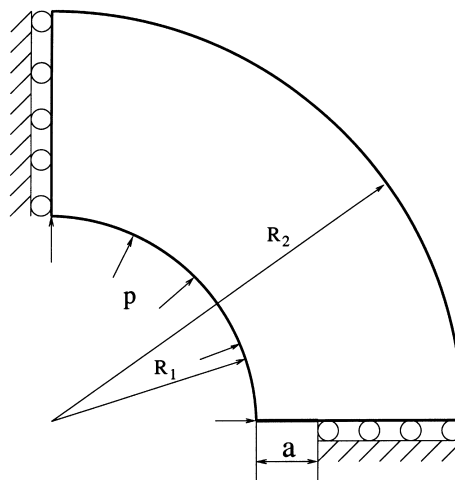


Fig. 17. Quarter portion of a hollow cylinder with symmetric horizontal cracks subjected to internal pressure loading.

### 6.5. Hollow cylinder with symmetric horizontal cracks at the inner face

Fig. 17 shows a quarter portion of a hollow cylinder with symmetric horizontal cracks at the inner face. The hollow cylinder has inner radius  $R_1 = 60$  mm, outer radius  $R_2 = 120$  mm, and the crack length is  $a = 15$  mm. The material is assumed to be elastic perfectly plastic with yield stress  $\sigma_Y = 4.0 \times 10^4$  MPa. The elastic properties are Young's modulus  $E = 3.0 \times 10^7$  MPa, and  $\nu = 0.3$ . The pressure loading is applied at the inner face of the cylinder (see Fig. 17), and the crack faces are assumed to be traction-free (i.e., there is no pressure applied to the crack faces). This is a simplified setting, which is used with the purposes of checking the effectiveness of the present computational scheme, and of comparing the CTO BEM, the CON BEM, and the FEM solution obtained with ABAQUS.

The BEM mesh is illustrated in Fig. 18. Note that the elements in the domain change orientation at the crack tip. Three contour integral paths are chosen for  $J$  integral evaluation. In order to verify the accuracy of the method used here, the above problem (see Fig. 17) has been solved with the commercial FEM program ABAQUS. The FEM mesh consists of 659 nodes and 114 8-noded quadratic elements (Q8), which includes 12 special elements at the crack tip region.

The calculation results are shown in Tables 6–8. Table 6 shows a comparison of the CTO and CON at various increments in terms of the number of iterations, CPU time, and residual norm (see Eq. (45)). Table 7 lists the average values of the  $J$  integral obtained with the CTO BEM, the CON BEM and the ABAQUS results. The BEM results for the  $J$  integral are the average obtained with the three  $J$  integral contours shown in Fig. 18. The relative error is calculated according to

$$\text{Error} = \frac{|J(\text{BEM}) - J(\text{ABAQUS})|}{J(\text{ABAQUS})} 100\%.$$

The results in Table 7 show that both the CTO and CON results agree well with the ABAQUS results. Table 8 shows a comparison of the  $J$  integral at various load levels and the corresponding  $J$  values at each of the contours shown in Fig. 18. Although the CON results for the  $J$  integral are very close to the CTO results, the number of iterations for the CTO BEM are much less than those for the CON BEM. This fact confirms the conclusion reached for the previous example.

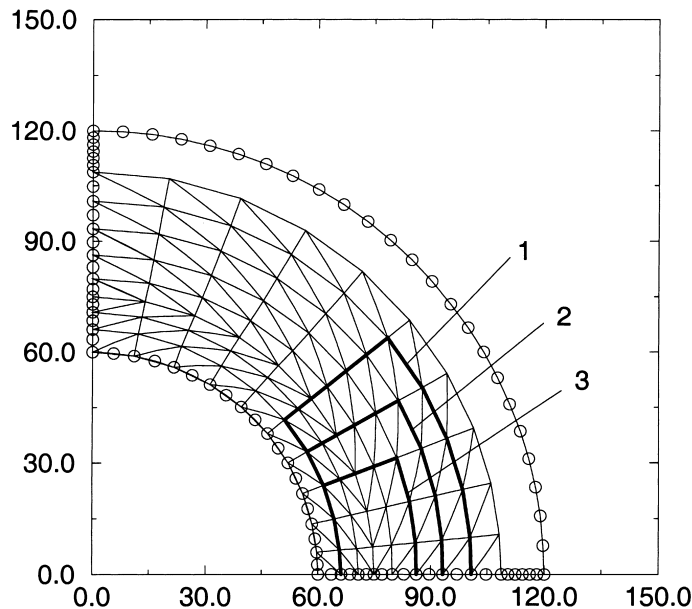


Fig. 18. BEM mesh for analysis of the hollow cylinder with symmetric horizontal cracks. The boundary discretization consists of 44 quadratic elements and 93 nodes (including five double nodes for the corners and the crack tip); the domain discretization consists of 160 elements (T6) and 357 nodes. The three bold contours are used for  $J$  integral evaluation.

Table 6  
Comparison of CTO BEM and CON BEM in 10 load steps,  $p = 14,000$  MPa

Load step	1–8	9	10
Iteration (CTO)	–	2	3
Iteration (CON)	–	5	6
CPU s (CTO) <sup>a</sup>	456.3	463.4	471.7
CPU s (CON) <sup>a</sup>	450.8	461.7	473.8
ResNorm (CTO)	9.2004E–12	3.6237E–10	1.1465E–11
ResNorm (CON)	9.2004E–12	2.5792E–10	1.5201E–10

<sup>a</sup>SGI workstation.

Table 7  
Comparison of  $J$  integrals (N/mm) with CTO BEM, CON BEM, and ABAQUS

Loading (MPa)	$J$ (CTO)	Error (%)	$J$ (CON)	Error (%)	$J$ (ABAQUS)
10,000	465.25	0.5	465.25	0.5	462.97
12,000	671.15	1.0	671.15	1.0	677.93
14,000	917.52	2.8	917.52	2.8	944.07
16,000	1223.00	3.7	1222.07	3.8	1270.00

Table 8  
 $J$  integral (N/mm) values of CTO BEM and CON BEM at three contour paths<sup>a</sup>

$J$ contour	10,000 MPa	12,000 MPa	14,000 MPa	16,000 MPa
1 (CTO)	516.60	745.24	1019.0	1359.3
2 (CTO)	463.38	668.51	914.14	1219.5
3 (CTO)	415.78	599.69	819.41	1090.2
1 (CON)	516.60	745.24	1019.0	1358.4
2 (CON)	463.38	668.51	914.14	1218.5
3 (CON)	415.78	599.69	819.41	1089.3

<sup>a</sup>The contour numbers are shown in Fig. 18.

## 7. Conclusions and extensions

The present study highlights the main features of the CTO and CON in the context of nonlinear constitutive relations and the BEM. It is worth noting that the CON becomes the special case of the CTO when the parameter  $\beta = 1$ , and  $\sigma_{n+1}^{(i)}$  at the  $i$ th iteration is computed from the nonconverged stress  $s_{n+1}^{(i-1)}$  at the previous iteration (rather than from the converged stress). Thus, use of the CON in conjunction with the RRA leads to loss of the quadratic rate of asymptotic convergence which characterizes Newton's iteration method. The CTO is also especially advantageous in sensitivity calculations [11,26].

Various examples have been presented, which include fracture problems and  $J$  integral evaluation. The numerical results support that the CTO is more powerful than the CON with respect to number of iterations, CPU time, residual norm, and convergence properties. For instance, in the first example of Section 6, the CTO achieves convergence in only one load step, while the CON needs six load steps (see Figs. 6–8).

Direct extension of the present work includes investigation of improved strategies for accurate evaluation of stresses at corner, e.g., using a Galerkin BEM [27], and use of other material models and criteria. This

work also has potential applications to nonlinear self-adaptive BEM with localized nonlinearity, which can be considered as an extension of previous work by Paulino et al. [27–30]. For instance, in an  $h$ -adaptive scheme, the initial mesh can be set as the boundary mesh only. As the analysis progresses, the boundary mesh is automatically refined, and as plasticity develops, new domain cells are automatically created. In this manner, elastoplastic problems could be solved efficiently (i.e., without unnecessary interior discretization) and without prior knowledge of the location and size of zones of nonlinearity (see Section 1). This topic is presently under investigation.

## Acknowledgements

This work was performed with supported from the National Science Foundation through Grant No. CMS-9713008 (Mechanics & Materials Program). The authors thank the Department of Civil and Environmental Engineering at the University of California, Davis, for hospitality while part of this work was developed. The authors also would like to thank Dr. Harrison Poon for providing them a version of his BEM CTO code.

## References

- [1] P.K. Banerjee, *The Boundary Element Methods in Engineering*, second ed., McGraw Hill, London, 1994.
- [2] H. Jin, K. Runesson, K. Matiasson, Boundary element formulation in finite deformation plasticity using implicit integration, *Comput. Struct.* 31 (1989) 25–34.
- [3] J.C.F. Telles, J.A.M. Carrer, Implicit procedures for the solution of elastoplastic problems by the boundary element method, *Math. Comput. Model* 15 (1991) 303–311.
- [4] J.C.F. Telles, J.A.M. Carrer, Static and transient dynamic nonlinear stress analysis by the boundary element method with implicit techniques, *Engrg. Anal. Boundary Elem.* 14 (1994) 65–74.
- [5] L.J. Leu, S. Mukherjee, Implicit objective integration for sensitivity analysis in nonlinear solid mechanics, *Int. J. Numer. Methods Engrg.* 37 (1994) 3843–3868.
- [6] L.J. Leu, S. Mukherjee, Sensitivity analysis of hyperelastic–viscoplastic solids undergoing large deformations, *Comput. Mech.* 15 (1994) 101–116.
- [7] L.J. Leu, S. Mukherjee, Sensitivity analysis in nonlinear solid mechanics by the boundary element method with an implicit scheme, *J. Engrg. Anal. Design* 2 (1995) 33–55.
- [8] A. Chandra, S. Mukherjee, *Boundary Element Methods in Manufacturing*, Oxford University Press, New York, 1997.
- [9] T.A. Cruse, *Boundary Element Analysis in Computational Fracture Mechanics*, Kluwer Academic Publishers, Dordrecht, 1988.
- [10] V.M.A. Leitão, *Boundary Elements in Nonlinear Fracture Mechanics*, Computational Mechanics Publications, Southampton, UK and Boston, USA, 1994.
- [11] M. Bonnet, S. Mukherjee, Implicit BEM formulations for usual and sensitivity problems in elastoplasticity using the consistent tangent operator concept, *Int. J. Solids Struct.* 33 (1996) 4461–4480.
- [12] H. Poon, S. Mukherjee, M. Bonnet, Numerical implementation of a CTO-based implicit approach for the BEM solution of usual and sensitivity problems in elastoplasticity, *Engrg. Anal. Boundary Elem.* 22 (1998) 257–269.
- [13] G.H. Paulino, Y. Liu, Elasto-viscoplastic consistent tangent operator-based implicit algorithm for boundary element methods (to be submitted for Journal publication).
- [14] J.C. Simo, R.L. Taylor, Consistent tangent operators for rate-independent elastoplasticity, *Comput. Methods Appl. Mech. Engrg.* 48 (1985) 101–118.
- [15] J.C. Simo, T.J.R. Hughes, *Computational Inelasticity*, Springer, New York, 1998.
- [16] W. Thomson [later Lord Kelvin], Note on the integration of the equations of equilibrium of an elastic solid, *Cambridge Dublin Math. J.* 3 (1848) 87–89.
- [17] G.H. Paulino, Novel formulations of the boundary element method for fracture mechanics and error estimation, Ph.D. Dissertation, Cornell University, Ithaca, New York, 1995.
- [18] W.H. Press, S.A. Teukolsky, W.T. Vetterling, B.P. Flannery, *Numerical Recipes: The Art of Scientific Programming*, second ed., Cambridge University Press, Cambridge, 1992.
- [19] M. Kleiber, T.D. Hien, E. Postek, Incremental finite-element sensitivity analysis for nonlinear mechanics applications, *Int. J. Numer. Methods Engrg.* 37 (1994) 3291–3308.
- [20] W.C. Carpenter, D.T. Read, R.H. Dodds, Comparison of several path independent integrals including plasticity effects, *Int. J. Fract.* 31 (1986) 303–323.
- [21] E.E. Gdoutos, *Fracture Mechanics Criteria and Applications*, Kluwer Academic Publishers, Dordrecht, The Netherlands, 1990.
- [22] J.R. Rice, A path independent integral and the approximate analysis of strain concentration by notches and cracks, *J. Appl. Mech. Trans. ASME* 35 (2) (1968) 379–386.

- [23] M. Bonnet, H. Poon, S. Mukherjee, Hypersingular formulation for boundary strain evaluation in the context of a CTO-based implicit BEM scheme for small strain elastoplasticity, *Int. J. Plasticity* 14 (10-11) (1998) 1033–1058.
- [24] Hibbitt, Karlsson and Sorensen, *ABAQUS/Standard – Verification Manual*, vol. I. Pawtucket, RI, 1997, Version 5.7..
- [25] T.K. Hellen, Virtual crack extension methods for nonlinear materials, *Int. J. Numer. Methods Engrg.* 28 (1989) 929–942.
- [26] C.A. Vidal, R.B. Haber, Design sensitivity analysis for rate-independent elastoplasticity, *Comput. Methods Appl. Mech. Engrg.* 107 (1993) 393–431.
- [27] G.H. Paulino, L.J. Gray, Galerkin residuals for adaptive symmetric-Galerkin boundary element methods, *J. Engrg. Mech. (ASCE)* 125 (5) (1999) 575–585.
- [28] G.H. Paulino, L.J. Gray, V. Zarikian, Hypersingular residuals – A new approach for error estimation in the boundary element method, *Int. J. Numer. Methods Engrg.* 36 (12) (1996) 2005–2029.
- [29] G.H. Paulino, F. Shi, S. Mukherjee, P. Ramesh, Nodal sensitivities as error estimates in computational mechanics, *Acta Mech.* 121 (1–4) (1997) 191–213.
- [30] G.H. Paulino, I.F.M. Menezes, J.B. Cavalcante Neto, L.F. Martha, A methodology for adaptive finite element analysis: Towards an integrated computational environment, *Comput. Mech.* 23 (5–6) (1999) 361–388.